nature physics

LETTERS

PUBLISHED ONLINE: 10 OCTOBER 2016 | DOI: 10.1038/NPHYS3905

Ultrastrong coupling of a single artificial atom to an electromagnetic continuum in the nonperturbative regime

P. Forn-Díaz[1,2,3*], J. J. García-Ripoll[4], B. Peropadre[5], J.-L. Orgiazzi[1,3,6], M. A. Yurtalan[1,3,6], R. Belyansky[1,6], C. M. Wilson[1,6*†] and A. Lupascu[1,2,3*†]

The study of light–matter interaction has led to important advances in quantum optics and enabled numerous technologies. Over recent decades, progress has been made in increasing the strength of this interaction at the single-photon level. More recently, a major achievement has been the demonstration of the so-called strong coupling regime[1,2], a key advancement enabling progress in quantum information science. Here, we demonstrate light–matter interaction over an order of magnitude stronger than previously reported, reaching the nonperturbative regime of ultrastrong coupling (USC). We achieve this using a superconducting artificial atom tunably coupled to the electromagnetic continuum of a one-dimensional waveguide. For the largest coupling, the spontaneous emission rate of the atom exceeds its transition frequency. In this USC regime, the description of atom and light as distinct entities breaks down, and a new description in terms of hybrid states is required[3,4]. Beyond light–matter interaction itself, the tunability of our system makes it a promising tool to study a number of important physical systems, such as the well-known spin-boson[5] and Kondo models[6].

Light propagating in a one-dimensional (1D) waveguide is described by a 1D electromagnetic field with a continuous spectrum of frequencies. The strong coupling regime[7] between an atom and such an electromagnetic continuum is defined as the regime in which the atom emits radiation predominantly into the waveguide with a rate Γ_G that significantly exceeds the decoherence rate of the atom as well as emission into any other channel. In this regime, the atomic transition frequency Δ far exceeds the emission rate $\Gamma_G \ll \Delta$. Achieving strong coupling to a continuum is a recent achievement in quantum optics[8]. Strong atom–waveguide coupling has numerous applications, such as the development of quantum networks[9] for quantum communication[10] and quantum simulation[11]. This technology, first demonstrated with superconducting qubits in open transmission lines[8,10,12,13], has also been implemented with both neutral atoms[14] and quantum dots[15] in photonic crystal waveguides. The distinctive signature of strong coupling is a decrease below 50% of the amplitude of transmitted signals due to coherent atomic scattering of photons.

A distinct regime of light–matter interaction is reached when Γ_G becomes comparable to the atomic transition frequency $\Gamma_G/\Delta \sim 0.1$, the ultrastrong coupling (USC) regime. Most studies involving atom-field interactions are in the regime $\Gamma_G \ll \Delta$, where the common rotating-wave approximation (RWA) applies. In the USC regime, the RWA breaks down but perturbative treatments still allow an effective atom-field description when $\Gamma_G/\Delta \sim 0.1$ (refs 16,17). A novel, unexplored regime of light–matter interaction is the nonperturbative USC regime, where Γ_G approaches or exceeds the atomic transition frequency $\Gamma_G/\Delta \sim 1$ and perturbation theory breaks down. This is a general definition also applicable to the case of discrete modes in cavity quantum electrodynamics systems[18]. We note that the nonperturbative USC regime has also been referred to in the literature as the deep strong coupling regime[19]. In the nonperturbative USC regime, the atom–photon system is described by photons dressing the atom even in the ground state[3,4,18]. In this regime, the Markovian approximation also breaks down because the broad qubit linewidth Γ_G implies that the spectral density of the environment seen by the atom is not independent of frequency. The presence of a continuum of modes ultrastrongly coupled to an atom has the additional effect of renormalizing the atomic frequency from the bare value Δ_0, which is a generalization of the well-known Lamb shift to arbitrary coupling strengths. These renormalization effects are also central to the well-known spin-boson model[5], which has been used to describe, for example, open quantum systems[20], quantum stochastic resonance[21] and phase transitions in Josephson junctions[22]. Reaching the nonperturbative USC regime allows the exploration of the ultimate limits in light–matter interaction strength and relativistic quantum information phenomena[23]. In addition, ultrastrong couplings may have technological applications, such as single-photon nonlinearities[24] and broadband single-photon sources[3].

Superconducting qubits are artificial atoms with transitions in the microwave range of frequencies. Recently, flux-type superconducting qubits have been put forward as candidates to reach the nonperturbative USC regime[3,25], having demonstrated large galvanic couplings to resonators[17] and a large anharmonicity that allows them to remain an effective two-level system when $\Gamma_G \sim \Delta$. This is in contrast to other more weakly anharmonic qubits whose transitions would overlap for large enough Γ_G.

Here, we demonstrate nonperturbative ultrastrong coupling of a superconducting flux qubit[26] coupled to an open 1D transmission line via a shared Josephson junction. As predicted[3,25], we observe that Γ_G increases with the inverse of the coupling junction size. For

[1]Institute for Quantum Computing, University of Waterloo, Waterloo N2L 3G1, Canada. [2]Department of Physics and Astronomy, University of Waterloo, Waterloo N2L 3G1, Canada. [3]Waterloo Institute for Nanotechnology, University of Waterloo, Waterloo N2L 3G1, Canada. [4]Instituto de Física Fundamental IFF-CSIC, Madrid 28006, Spain. [5]Department of Chemistry and Chemical Biology, Harvard University, Cambridge, Massachusetts 02138, USA. [6]Department of Electrical and Computer Engineering, University of Waterloo, Waterloo N2L 3G1, Canada. †These authors contributed equally to this work. *e-mail: pforndiaz@uwaterloo.ca; chris.wilson@uwaterloo.ca; adrian.lupascu@uwaterloo.ca

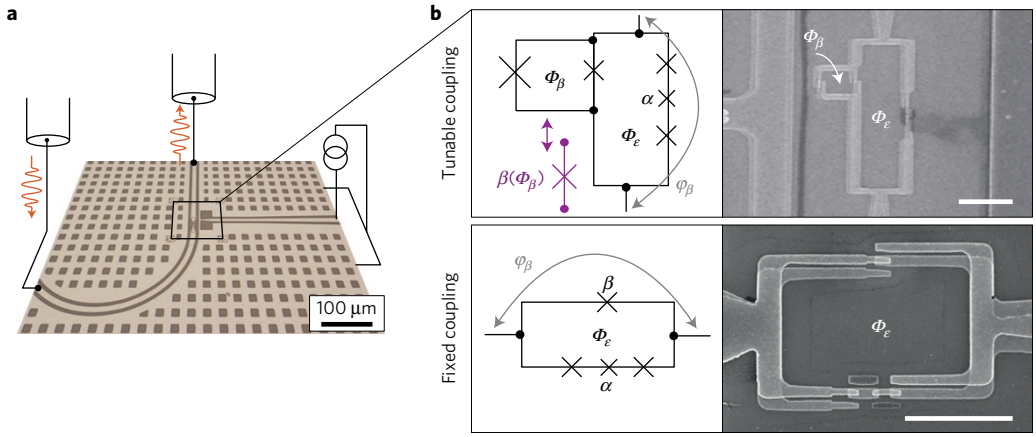

Figure 1 | Measurement set-up and devices. a, Schematic of the circuit layout, with a micrograph of a section of a chip containing a transmission line and a flux qubit. **b**, Circuit schematic of a flux qubit coupled to a transmission line with tunable (fixed) coupling shown at the top (bottom). In both cases, the coupling is proportional to the matrix element of the phase operator φ_β across the coupling junction β. The scanning-electron micrographs show the corresponding circuits. The white scale bars are 4 μm.

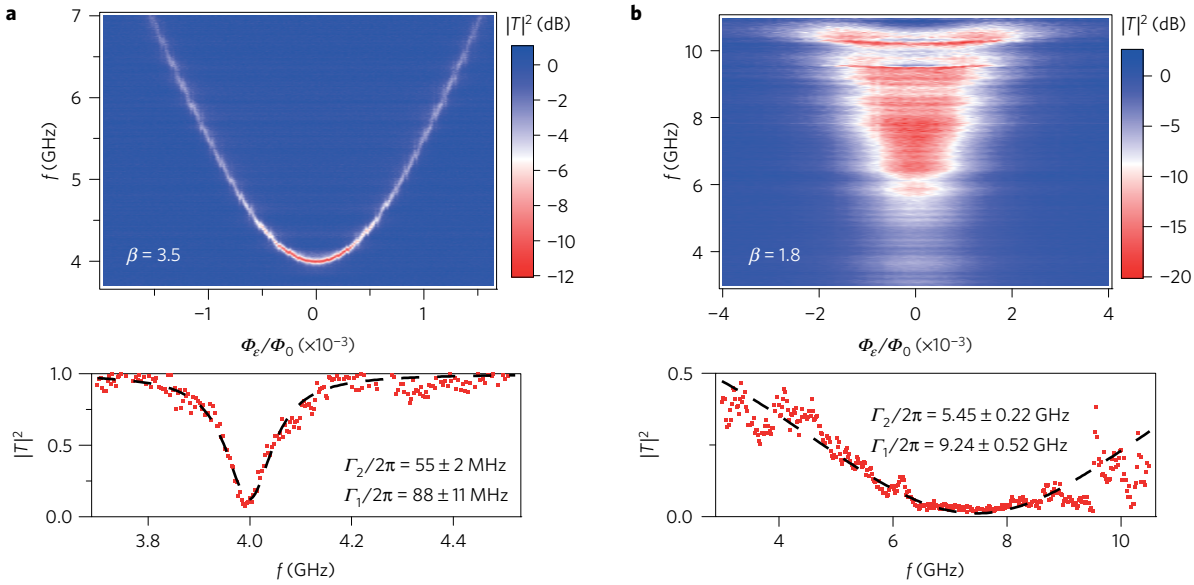

Figure 2 | Spectroscopy of devices with fixed coupling. a,**b**, Plots showing transmission versus frequency and magnetic flux referenced to $\Phi_0/2$, with individual traces showing transmission corresponding to the magnetic flux at the minimum qubit splitting. Dashed lines are fits to equation (1). Bounds on Γ_1 are from considerations of thermal effects (Methods). **a**, Transmission spectrum of qubit with $\beta \simeq 3.5$ and gap $\Delta/2\pi = 3.996 \pm 0.001$ GHz. The 95% extinction on-resonance indicates strong coupling. **b**, Spectrum of qubit with $\beta \simeq 1.8$. The fit yields $\Gamma_1/2\pi \simeq 9.24 \pm 0.52$ GHz, exceeding the qubit gap of $\Delta/2\pi = 7.68 \pm 0.08$ GHz. This implies $\Gamma_1/\Delta = 1.20 \pm 0.07$, which indicates ultrastrong coupling. The extinction of the transmitted power at the symmetry point is 97%.

devices with a small-enough coupling junction we measure $\Gamma_G \sim \Delta$, indicating that we reach the nonperturbative USC regime. Our flux qubit has four Josephson junctions. Two reference junctions are designed with the same area, while the areas of the other two junctions are scaled by the factors $\alpha \sim 0.6$ and $\beta > 1$ with respect to the area of the reference junctions[27]. The flux qubit is galvanically attached to the centre line of a 1D coplanar waveguide transmission line (Fig. 1a). To achieve ultrastrong couplings, we place the β-junction in parallel to the other three (Fig. 1b). The coupling to the line is then mainly determined[3,25] by the matrix element between ground $|0\rangle$ and excited $|1\rangle$ qubit states of the superconducting phase operator across the β-junction $\langle 0|\hat{\varphi}_\beta|1\rangle \equiv \varphi_\beta$, which is the dominant contribution to the coupling for $\beta < 4$. Further, we make the coupling tunable by turning the β-junction into a superconducting quantum interference device (SQUID) threaded by a flux Φ_β, as shown in Fig. 1b (Methods).

The experiments are performed by applying a probe field with a variable frequency and recording the transmitted field amplitude and phase on a vector network analyzer. For emission rates $\Gamma_1/\Delta \ll 1$, where Γ_1 is the total emission rate and, in the presence of thermal excitations, the transmitted coherent scattering amplitude at low driving power is given by[8,28]:

$$T = 1 + R \approx \frac{1 + (\delta\omega/\Gamma_2)^2 + r_0(i\delta\omega/\Gamma_2 - 1)}{1 + (\delta\omega/\Gamma_2)^2} \qquad (1)$$

Here $\Gamma_2 \equiv \Gamma_\varphi + (\Gamma_1/2)(1 + 2n_{\rm th})$ is the total decoherence rate, Γ_φ is the pure dephasing rate, $\delta\omega = \omega - \Delta$ is the detuning of the probe field, and $n_{\rm th}$ is the thermal photon occupation number at the qubit frequency (Supplementary Information). The maximum reflection amplitude is $r_0 = \Gamma_1/[2\Gamma_2(1 + 2n_{\rm th})]$. As in other experiments on superconducting quantum circuits[8,10], relaxation into channels other

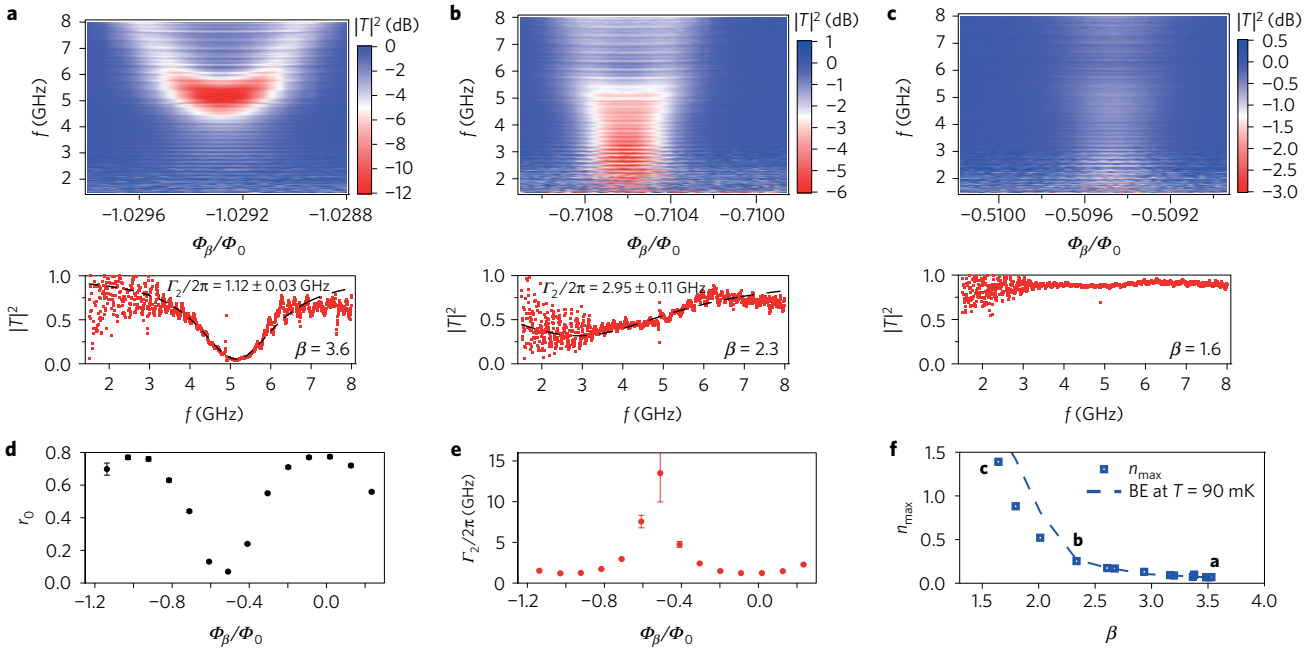

Figure 3 | Tunable ultrastrong coupling device. a–c, Colour plots of transmission versus frequency and magnetic flux (top) and line plots at the magnetic flux corresponding to the minimum qubit splitting (bottom). Dashed lines are fits to equation (1). As a function of the applied magnetic field we observe a transition from strong (**a**) to nonperturbative ultrastrong coupling (**b**,**c**). **a**, For $\Phi_\beta/\Phi_0 \simeq -1$ the coupling is lowest (β largest) and the extinction is 95% of the transmitted power. **b**, At $\Phi_\beta/\Phi_0 \simeq -0.71$ the qubit reaches $\Gamma_1 \simeq \Delta$. **c**, Near $\Phi_\beta/\Phi_0 \simeq -0.5$ the system reflects only 10% of the incoming power and shows little signature of frequency dependence. The measured normalized couplings Γ_1/Δ are 0.35 (**a**), 0.90 (**b**) and >1.5 (**c**), respectively. The large oscillations observed below 4 GHz are caused by reflections outside of our optimal measurement bandwidth 4–8 GHz. **d**,**e**, Fitting equation (1) at the symmetry point of each qubit resonance allows extraction of the modulation of r_0 **d** and Γ_2 **e**. Error bars represent the uncertainty in the fitted values of r_0 and Γ_2. From these values, we can compute bounds for Γ_1 and the maximum thermal photon number n_{max} (see Methods). **f**, Extracted n_{max}, showing thermal excitation at lower β (lower frequency). Size of markers includes error bars. The decreasing value of Δ below $\sim$5 GHz causes the photon occupation to increase exponentially, closely following a Bose–Einstein (BE) distribution at $T_{eff} = 90$ mK (dash-dotted line) for $\beta > 2$. The particular resonances shown in **a**–**c** are indicated.

than the waveguide is negligible. Therefore, we assume $\Gamma_1 = \Gamma_G$. We note that equation (1) applies in the RWA. However, it has recently been shown[4] that the scattering lineshapes are approximately Lorentzian in the USC regime up to $\Gamma_1/\Delta \sim 1$ if we consider Δ and Γ_1 to be renormalized parameters. This can be shown using a polaron transformation, allowing us to interpret the scattering centre as an atom dressed by a cloud of photons.

We first show measurements on a device with a fixed coupling junction with $\beta \simeq 3.5$ (Fig. 1b). The transmission spectrum as a function of applied magnetic field (Fig. 2a) shows a maximum extinction at the symmetry point of 95%, indicating strong coupling. By fitting equation (1) (dashed line), we infer $\Gamma_1/2\pi = 88 \pm 11$ MHz (see Methods), $\Delta/2\pi = 3.996 \pm 0.001$ GHz, giving $\Gamma_1/\Delta = 0.02$, which is not in the USC regime. Flux qubit spectra in transmission lines similar to this one have previously been reported[8,29].

To enhance the coupling strength, we designed a second device where the size of the β-junction was decreased to $\beta \simeq 1.8$. The resulting qubit spectrum in Fig. 2b shows striking differences compared to the previous device with $\beta \simeq 3.5$. The qubit linewidth at the symmetry point is very large, comparable to the total measurement bandwidth of 3–11 GHz. The deviations from a Lorentzian lineshape are due to bandwidth limitations of our set-up, still allowing us to infer a full-width at half-maximum of $2\Gamma_2/2\pi \simeq 10.90 \pm 0.44$ GHz (see Methods). The extracted qubit emission rate $\Gamma_1/2\pi \simeq 9.24 \pm 0.52$ GHz exceeds the qubit splitting $\Delta/2\pi = 7.68 \pm 0.08$ GHz, giving $\Gamma_1/\Delta = 1.20 \pm 0.07$, a clear indication that this device reaches the nonperturbative USC regime.

Having observed two devices with $\Gamma_1 \ll \Delta$ and $\Gamma_1 > \Delta$, we now explore the intermediate region using a device with tunable coupling (Fig. 1b) designed with a tunable range of $\beta \sim 1.6$–3.6. In Fig. 3a–c, spectroscopy of the tunable coupling device is shown at three different values of Φ_β. Using scanning-electron microscope (SEM) images of the measured device, we identify Fig. 3a–c as effectively having, respectively, $\beta_{(a)} \simeq 3.6$, $\beta_{(b)} \simeq 2.3$, $\beta_{(c)} \simeq 1.6$. Figure 3a corresponds to the highest effective β-junction size, therefore the lowest coupling strength. A flux qubit spectrum can be identified with $\Delta/2\pi = 5.20 \pm 0.02$ GHz and $2\Gamma_2/2\pi \simeq 2.40 \pm 0.07$ GHz. The maximum extinction at the symmetry point is over 95%. The quality of the signal below 4 GHz degrades due to the measurement taking place outside the optimal bandwidth of our amplifier and circulators (4–8 GHz, Supplementary Information). In Fig. 3b, the qubit gap decreases to $\Delta/2\pi \simeq 2.90 \pm 0.05$ GHz, as expected for a smaller β-junction. The width $2\Gamma_2/2\pi = 5.90 \pm 0.22$ GHz is clearly enhanced, with the extinction decreasing to 30%. In Fig. 3c, the qubit spectrum is barely discernible. The extinction is only 10%, with a response that appears featureless in our frequency range. Figure 3d,e shows the extracted values of r_0 and Γ_2 using equation (1). The value of $2\Gamma_2/2\pi \simeq 13 \pm 3$ GHz from Fig. 3c is an inferred bound due to the difficulty in fitting the transmission at this value of flux.

To understand the spectrum of the tunable coupling device and extract the corresponding emission rates Γ_1, we need to take into account finite temperature effects. We can set an upper bound on n_{th}, which is $n_{max} \equiv (1/2)(1/\sqrt{r_0} - 1)$ (Methods). Figure 3f shows that the values of n_{max} for $\beta > 2$ are consistent with a unique maximum effective temperature of $T_{eff} = 90$ mK, comparable to other superconducting qubit experiments. Using $0 < n_{th} < n_{max}$, we then put bounds on Γ_1: $2\Gamma_2 r_0 < \Gamma_1 < 2\Gamma_2\sqrt{r_0}$. Using these bounds, we plot Γ_1/Δ in Fig. 4a. The plot clearly shows that we can tune the device from the regime of strong coupling all the way into the nonperturbative USC regime. The curve in Fig. 4a

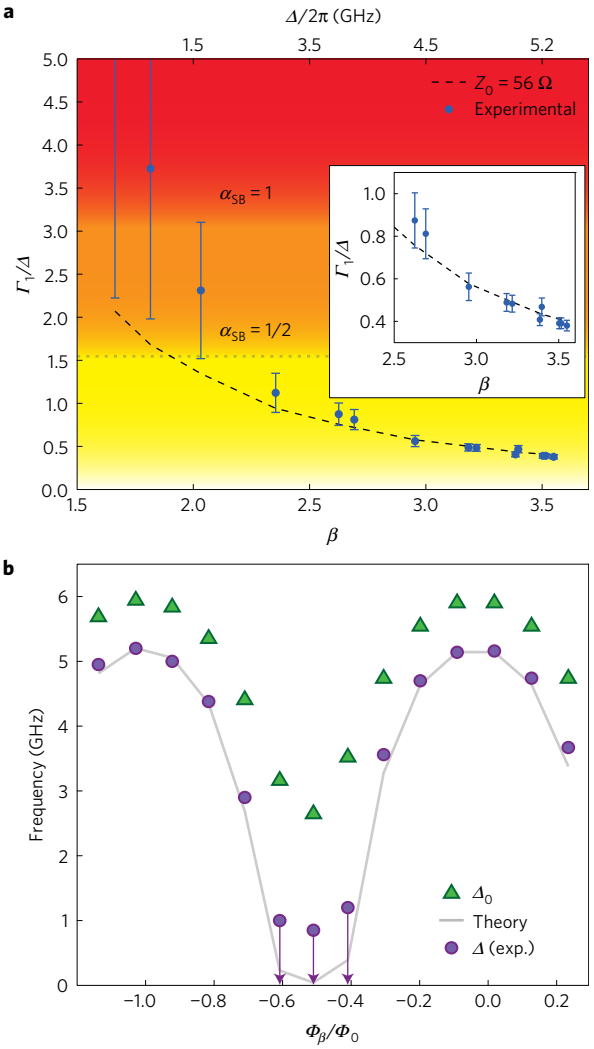

Figure 4 | Normalized coupling rates and frequency renormalization. **a**, Experimental normalized coupling rate Γ_1/Δ (dots) as a function of the coupling junction size β for the device with tunable coupling. Error bars correspond to systematic bounds on Γ_1 (see Methods). The dashed curve represents the calculated parameter Γ_1/Δ from equation (2). There is very good agreement with the data for an impedance close to the nominal 50 Ω. The coloured regions indicate the spin-boson model regimes where the qubit dynamics are underdamped, overdamped and localized. The inset shows an enlargement of the high-β region. For $\beta < 2$ the curve represents a lower bound. **b**, Observed qubit frequency Δ at the symmetry point (circles) as a function of Φ_β, along with calculated bare qubit gaps Δ_0 (triangles). The curve is the theoretical prediction for the renormalized qubit gaps calculated using equation (3) assuming a cutoff frequency of $\omega_C/2\pi = 50$ GHz. Near integers of Φ_β/Φ_0, the coupling to the line is minimum and the observed Δ follows the shape of the calculated Δ_0, with an offset. Near $\Phi_\beta/\Phi_0 \sim -0.5$, the difference between Δ and Δ_0 increases substantially. This is the region of nonperturbative ultrastrong coupling and the suppression of Δ is consistent with the renormalization effects predicted by the spin-boson model. The spectra in this region are difficult to fit with a Lorentzian and upper bounds to the frequency indicated by arrows are drawn instead.

corresponds to the theoretical value of the normalized coupling strength (Supplementary Information)

$$\Gamma_1/\Delta \simeq \frac{1}{2\pi}\frac{R_Q}{Z_0}|\varphi_\beta|^2 \qquad (2)$$

with $R_Q = h/(2e)^2 = 6.5$ kΩ the resistance quantum and Z_0 the characteristic impedance of the line. The matrix element values of the phase operator across the coupling junction β, $|\varphi_\beta|^2$, are calculated using the methods of ref. 3. The observed values of Γ_1/Δ agree very well with the calculated values based on our circuit[3] for an impedance close to the nominal 50 Ω. Above $\Gamma_1/\Delta \simeq \pi/2$, equation (2) becomes a lower bound (Supplementary Information). This is consistent with data in the range $\beta < 2$ lying above equation (2). Including renormalization effects[5] in equation (2) might further improve the agreement with the measurements for $\beta < 2$.

Our system allows us to explore the spin-boson (SB) model in an ohmic bath. According to the SB model, the high-frequency modes of the transmission line renormalize the bare qubit splitting Δ_0 to[4,5]

$$\Delta = \Delta_0(p\Delta_0/\omega_C)^{\alpha_{SB}/(1-\alpha_{SB})} \qquad (3)$$

α_{SB} is the SB normalized coupling strength that is related to the spectral density of the environment $J(\omega)$. For an ohmic system such as our transmission line, $\alpha_{SB} = J(\omega)/\pi\omega$. $\omega_C \gg \Delta_0$ is the cutoff frequency of the environment and p is a constant of order 1. Up to $\alpha_{SB} \sim 0.5$, we identify $\alpha_{SB} = \Gamma_1/\pi\Delta$. Above $\alpha_{SB} \simeq 0.5$ (or $\Gamma_1/\Delta \simeq \pi/2$) this relation becomes a lower bound for α_{SB} (Supplementary Information). In Fig. 4b we plot the experimental qubit splittings Δ (circles). Using qubit junction dimensions extracted from SEM images of the device, we diagonalize the qubit Hamiltonian at each flux Φ_β (triangles) to give the bare qubit gaps Δ_0. We then renormalize the calculated Δ_0 using equation (3) and a value of $p = \exp(1+\gamma) \simeq 4.8$, which is derived using an exponential cutoff model[4,5]. γ is the Euler constant. We find the best fit to the measured Δ using a cutoff of $\omega_C/2\pi = 50$ GHz, which is consistent with characteristic system frequencies such as the plasma frequency of the qubit junctions and the superconducting gap. The agreement between the observed qubit splittings Δ and our estimates of the renormalized gaps is clear[3–5].

As a prelude to future work, we can place our results in the context of the SB model. The SB model defines three dynamical regimes for the qubit: underdamped ($\alpha_{SB} < 0.5$), overdamped ($1 > \alpha_{SB} > 0.5$) and localized ($\alpha_{SB} > 1$). The connection between Γ_1/Δ and α_{SB} allows us to draw the boundaries between these regimes in Fig. 4a. We see that our tunable device enters well into the overdamped regime, and very possibly into the localized regime for $\beta < 2$. More detailed measurements of the dynamics of the device in these regimes could further confirm the predictions of the SB model. Suggestively, the strong reduction of the qubit response seen in Fig. 3c (leftmost data points in Fig. 4a) with a flat response as a function of frequency is consistent with simulations of classical double-well dynamics in the overdamped regime (P. Forn-Díaz, manuscript in preparation).

We have presented measurements of superconducting flux qubits in 1D open transmission lines in regimes of interaction starting at strong coupling and ranging deeply into the ultrastrong coupling regime. In particular, we observed qubits with emission rates exceeding their own frequency, a clear indication of nonperturbative ultrastrong coupling. These results are very relevant for the study of open systems in the USC regime, opening the door to the development of a new generation of quantum electronics with ultrahigh bandwidth for quantum and nonlinear optics applications. The tunability of our system also makes it well-suited to the simulation of other quantum systems. In particular, we showed that the device can span the various transition regions of the SB model. With further development of our quantum circuit, the structure of the photon dressing cloud could also be directly detected, allowing the study of the physics of the Kondo model[6] in a well-controlled setting. The ultrastrong coupling regime has other interesting intrinsic properties on its own, such as the entangled nature of the ground state.

Note added in proof: After acceptance of our paper, a related manuscript was published[30] showing similar results to this work using a resonator instead of a transmission line.

Methods

Methods, including statements of data availability and any associated accession codes and references, are available in the online version of this paper.

Received 24 January 2016; accepted 1 September 2016; published online 10 October 2016

References

1. Haroche, S. & Raimond, J.-M. *Exploring the Quantum: Atoms, Cavities, and Photons* (Oxford Univ. Press, 2006).
2. Wallraff, A. *et al*. Circuit quantum electrodynamics: coherent coupling of a single photon to a Cooper pair box. *Nature* **431,** 162–167 (2004).
3. Peropadre, B., Zueco, D., Porras, D. & García-Ripoll, J. J. Nonequilibrium and nonperturbative dynamics of ultrastrong coupling in open lines. *Phys. Rev. Lett.* **111,** 243602 (2013).
4. Díaz-Camacho, G., Bermudez, A. & García-Ripoll, J. J. Dynamical polaron ansatz: a theoretical tool for the ultra-strong coupling regime of circuit QED. *Phys. Rev. A* **93,** 043843 (2016).
5. Leggett, A. J. *et al*. Dynamics of the dissipative two-state system. *Rev. Mod. Phys.* **59,** 1–85 (1987).
6. Le Hur, K. Kondo resonance of a microwave photon. *Phys. Rev. B* **85,** 140506 (2012).
7. Shen, J.-T. & Fan, S. Coherent single photon transport in a one-dimensional waveguide coupled with superconducting quantum bits. *Phys. Rev. Lett.* **95,** 213001 (2005).
8. Astafiev, O. *et al*. Resonance fluorescence of a single artificial atom. *Science* **327,** 840–843 (2010).
9. Kimble, H. J. The quantum internet. *Nature* **453,** 1023–1030 (2008).
10. Hoi, I.-C. *et al*. Demonstration of a single-photon router in the microwave regime. *Phys. Rev. Lett.* **107,** 073601 (2011).
11. García-Álvarez, L. *et al*. Fermion–fermion scattering in quantum field theory with superconducting circuits. *Phys. Rev. Lett.* **114,** 070502 (2015).
12. Hoi, I.-C. *et al*. Giant cross-Kerr effect for propagating microwaves induced by an artificial atom. *Phys. Rev. Lett.* **111,** 053601 (2013).
13. van Loo, A. F. *et al*. Photon-mediated interactions between distant artificial atoms. *Science* **342,** 1494–1496 (2013).
14. Goban, A. *et al*. Superradiance for atoms trapped along a photonic crystal waveguide. *Phys. Rev. Lett.* **115,** 063601 (2015).
15. Arcari, M. *et al*. Near-unity coupling efficiency of a quantum emitter to a photonic crystal waveguide. *Phys. Rev. Lett.* **113,** 093603 (2014).
16. Niemczyk, T. *et al*. Circuit quantum electrodynamics in the ultrastrong-coupling regime. *Nat. Phys.* **6,** 772–776 (2010).
17. Forn-Díaz, P. *et al*. Observation of the Bloch–Siegert shift in a qubit-oscillator system in the ultrastrong coupling regime. *Phys. Rev. Lett.* **105,** 237001 (2010).
18. Ciuti, C., Bastard, G. & Carusotto, I. Quantum vacuum properties of the intersubband cavity polariton field. *Phys. Rev. B* **72,** 115303 (2005).
19. Casanova, J. *et al*. Deep strong coupling regime of the Jaynes–Cummings model. *Phys. Rev. Lett.* **105,** 263603 (2010).
20. Grifoni, M., Paladino, E. & Weiss, U. Dissipation, decoherence and preparation effects in the spin-boson system. *Eur. Phys. J. B* **10,** 719–729 (1999).
21. Gammaitoni, L., Hänggi, P., Jung, P. & Marchesoni, F. Stochastic resonance. *Rev. Mod. Phys.* **70,** 223–287 (1998).
22. Penttilä, J. S., Parts, U., Hakonen, P. J., Paalanen, M. A. & Sonin, E. B. Superconductor–insulator transition in a single Josephson junction. *Phys. Rev. Lett.* **82,** 1004–1007 (1999).
23. Sabín, C., Peropadre, B., Rey, M. D. & Martín-Martínez, E. Extracting past-future vacuum correlations using circuit QED. *Phys. Rev. Lett.* **109,** 033602 (2012).
24. Sánchez-Burillo, E., Zueco, D., García-Ripoll, J. J. & Martín-Moreno, L. Scattering in the ultrastrong regime: nonlinear optics with one photon. *Phys. Rev. Lett.* **113,** 263604 (2014).
25. Bourassa, J. *et al*. Ultrastrong coupling regime of cavity QED with phase-biased flux qubits. *Phys. Rev. A* **80,** 032109 (2009).
26. Mooij, J. E. *et al*. Josephson persistent-current qubit. *Science* **285,** 1036–1039 (1999).
27. Orgiazzi, J. L. *et al*. Flux qubits in a planar circuit quantum electrodynamics architecture: quantum control and decoherence. *Phys. Rev. B* **93,** 104518 (2016).
28. Peropadre, B. *et al*. Scattering of coherent states on a single artificial atom. *New J. Phys.* **15,** 035009 (2013).
29. Haeberlein, M. *et al*. Spin-boson model with an engineered reservoir in circuit quantum electrodynamics. Preprint at https://arxiv.org/abs/1506.09114 (2015).
30. Yoshihara, F. *et al*. Superconducting qubit–oscillator circuit beyond the ultrastrong-coupling regime. *Nat. Phys.* http://dx.doi.org/10.1038/nphys3906 (2016).

Acknowledgements

We acknowledge financial support from NSERC of Canada, the Canadian Foundation for Innovation, the Ontario Ministry of Research and Innovation, Industry Canada, Canadian Microelectronics Corporation, EU FP7 FET-Open project PROMISCE, Spanish Mineco Project FIS2012-33022 and CAM Network QUITEMAD+. B.P. acknowledges the Air Force of Scientific Research for support under award FA9550-12-1-0046. The University of Waterloo's Quantum NanoFab was used for this work. We thank A. J. Leggett and A. Garg for fruitful discussions, and M. Otto, S. Chang, A. M. Vadiraj and C. Deng for help with device fabrication and with the measurement set-ups.

Author contributions

P.F.-D., C.M.W. and A.L. designed the experiment. P.F.-D. designed the devices and fabricated them. P.F.-D., C.M.W. and A.L. conducted the experiments. J.-L.O. provided input to device design and fabrication. M.A.Y. and R.B. assisted in numerical modelling of devices. J.J.G.-R. and B.P. provided theoretical support to interpret the measurements. P.F.-D., C.M.W. and A.L. performed the data analysis and wrote the manuscript with feedback from all authors. C.M.W. and A.L. supervised the project.

Additional information

Supplementary information is available in the online version of the paper. Reprints and permissions information is available online at www.nature.com/reprints. Correspondence and requests for materials should be addressed to P.F.-D. or C.M.W. or A.L.

Competing financial interests

The authors declare no competing financial interests.

Methods

Device details and fabrication. We made the device with tunable coupling by replacing the β-junction with a SQUID threaded by a flux Φ_β. The tunable coupling device then consists of two loops, the main loop that changes primarily the qubit magnetic energy through the flux Φ_ϵ and the β-loop that changes the effective coupling to the transmission line through Φ_β. Changing β also modifies the minimum qubit splitting Δ. To minimize this effect, we make the SQUID junctions asymmetric, which lowers the sensitivity of Δ to Φ_β. Similar tunable coupling architectures were already suggested in ref. 31. In the experiment, we sweep the global magnetic field, therefore simultaneously changing Φ_ϵ and Φ_β. The qubit spectrum shows minima near $\Phi_\epsilon \approx \Phi_0(1/2+n)$, with $\Phi_0 = h/2e$ the quantum of flux, n being an integer (Supplementary Information). Here, different n will correspond to different Φ_β, leading to different coupling strengths. The loop areas A_ϵ/A_β are designed to have a large, incommensurate ratio, allowing the exploration of many different values of β.

The fabrication methods used are based on those of ref. 27. The fabrication of devices starts by patterning the transmission line using optical lithography followed by an evaporation of 200 nm of aluminium. A gap in the transmission line is left to place the qubit in a second lithography stage. We pattern the qubit using an electron beam writer. Prior to the second aluminium evaporation an Ar milling step is applied to remove the native oxide on the first aluminium layer, guaranteeing optimal conduction between the two aluminium layers. The qubit is evaporated using double-angle shadow mask evaporation, resulting in a total thickness of 105 nm. After the first shadow evaporation step, we oxidize the film with dynamical flow at $\sim$0.01 mbar for 7 min, yielding critical current densities of $\sim 12\,\mu\mathrm{A}\,\mu\mathrm{m}^{-2}$. The chip is then diced and the transmission line is wire-bonded to a printed circuit board connecting to the rest of the circuitry in our cryostat.

The transmission line consists of a 6.5 mm long on-chip coplanar waveguide with a centre line and gaps 8 μm and 4 μm wide, respectively, resulting in a 50 Ω characteristic impedance. Numerical simulations are run to verify the impedance of the circuit. We use a squared webbed ground to reduce superconducting vortex motion on the ground plane.

Bounds on qubit emission rate. The dependence of r_0 and Γ_2 on n_{th} shown below equation (1) does not allow the independent extraction of all parameters, $\Gamma_1, \Gamma_\varphi, n_{\mathrm{th}}$ at each value of β. However, we can set bounds on n_{th}. The lower bound case assumes no thermal excitations, therefore $n_{\mathrm{th}} = 0$. If we instead set $\Gamma_\varphi = \Gamma_2(1 - r_0(1+2n_{\mathrm{th}})^2) \geq 0$, we identify an upper bound on the photon occupation number $n_{\max} \equiv (1/2)(1/\sqrt{r_0} - 1)$. In Fig. 3f, the values of $n_{\max}$ were extracted assuming $\Gamma_\varphi = 0$. If we were to assume $\Gamma_\varphi/2\pi = 17$ MHz as the nonthermal dephasing rate, extracted from the narrower linewidth of the device in Fig. 2a assuming $n_{\mathrm{th}} = 0$, the resulting n_{th} would not differ significantly from $n_{\max}$. Now, bounds on $\Gamma_1 = 2\Gamma_2 r_0(1+2n_{\mathrm{th}})$ can be set as $\Gamma_1(n_{\mathrm{th}} = 0)$ and $\Gamma_1(n_{\mathrm{th}} = n_{\max})$, giving $2\Gamma_2 r_0 < \Gamma_1 < 2\Gamma_2\sqrt{r_0}$. The lower bound, $n_{\mathrm{th}} = 0$, is close to the calculated value of n_{th} at the cryostat temperature of 10 mK for all qubit frequencies.

Spectroscopic analysis. In all data shown, we use equation (1) to simultaneously fit the real and imaginary parts of the transmission. Supplementary Section 3 shows the full set of fitted resonances used in Figs 3 and 4 of the main text. Note that the baseline is fixed to a normalized value of 1 and is not adjusted. The baseline value is itself determined by measuring the transmitted background when the qubit is flux-tuned away from the frequency band of interest.

Data availability. The data that support the plots within this paper and other findings of this study are available from the corresponding authors upon request.

References

31. Peropadre, B., Forn-Díaz, P., Solano, E. & García-Ripoll, J. J. Switchable ultrastrong coupling. *Phys. Rev. Lett.* **105,** 023601 (2010).